Segmentation and Classification of Airborne GNSS-R Reflectivity Signals with Speckle Noise Mitigation

Sarah El Hajj Chehade, Hamza Issa, Georges Stienne, Serge Reboul

Segmentation and Classification of Airborne GNSS-R Reflectivity Signals with Speckle Noise Mitigation

Sarah El Hajj Chehade
LISIC
Universite Littoral Cote d'Opale
Calais, France
0009-0005-3008-9987

Hamza Issa
LISIC
Universite Littoral Cote d'Opale
Calais, France
0000-0003-3822-0394

Georges Stienne
LISIC
Universite Littoral Cote d'Opale
Calais, France
0000-0002-6757-8611

Serge Reboul
LISIC
Universite Littoral Cote d'Opale
Calais, France
0000-0002-2278-6134

***Abstract*—This article is dedicated to the study of Global Navigation Satellite System Reflectometry (GNSS-R) techniques for remote sensing applications, focusing on classifying the reflectivity of airborne signals to differentiate reflective surfaces along satellite traces. We propose an automatic segmentation algorithm using an online change point detector and off-line change point localization estimate. Given the presence of speckle noise in GNSS signals, a homomorphic log-transformation is applied to mitigate this noise. The system is shown to detect different land-forms in real flight experiments in France, using K-means clustering to identify sand, water bodies, and plain land.**

***Index Terms*—GNSS-R, Speckle noise, Homomorphic transformation, Change point detection, Change point localization.**

I. Introduction

The evolution of Global Navigation Satellite Systems (GNSS) has significantly expanded the scope of remote sensing applications for Earth surface and atmosphere monitoring. The Global Navigation Satellite System Reflectometry (GNSS-R) methodologies provide regional and global coverage and facilitates Earth Observation purposes through providing data from remote and inaccessible terrains through the use of refracted, reflected, and dispersed GNSS signals. The unique features of GNSS signals, particularly the use of L-band frequencies, keep them highly suitable for diverse remote sensing applications [1]. In recent years, GNSS-R has become a reliable remote sensing technology, providing precise measurements of important surface characteristics with a high level of temporal resolution and wide coverage [2]–[4]. The wide range of applications showcases its adaptability, from estimating wind speed [5], [6] to measuring ocean salinity [7], monitoring sea levels [8], [9], and assessing the cryosphere on land for aims like detecting sea ice [10], [11] and estimating snow depth [12], [13]. GNSS-R applications in land observation focus mainly on detecting in-land water bodies [14], [15], determining plant biomass [16], and measuring soil moisture [17], [18].

In this study, we apply GNSS-R techniques for detecting, monitoring, and characterizing in-land water bodies in regions at risk of flooding, using airborne GNSS-R observations [14]. This approach aligns with the growing interest in utilizing GNSS-R for local and regional scale studies, such as UAV-based GNSS-R sensors for water body surface measurement in flood monitoring operations [19], [20].

In GNSS-R remote sensing applications, accurate detection and localization of changes between different reflecting surfaces are critical. To address this, we employ change point detection algorithms on airborne GNSS-R data. However, challenges arise due to the presence of multiplicative noise, speckle noise, which deviates from the usual assumption of additive noise [14], [21].

In this work, we delve into the statistical modeling of speckle noise, specifically the Log-Gamma distribution, to enhance change point detection in GNSS-R reflectivity. Our method involves a homomorphic log-transformation of the reflectivity, resulting in a Log-Gamma distribution with constant variance. Using the Cumulative Sum (CUSUM) method and a Weighted Moving Average filter, our sequential change point detector effectively identifies changes in log-transformed reflectivity. The threshold for the CUSUM method is established by considering the Average Run Length ARL(0) for effective control of the false alarm rate. After

The authors would like to thank the CPER IDEAL program.

979-8-3503-8078-1/24/$31.00 ©2024 IEEE

detecting the change, we employ the maximum likelihood estimate, using the Log-Gamma distribution for analysis, to determine the time of occurrence. The methodology is validated using real flight data recorded in Northern France in 2020 and 2021, demonstrating the radar system's capacity to consistently differentiate reflecting surfaces using the classical K-means approach.

This article is structured as follows: In Section 2, we present our proposed statistical model, focusing on the homomorphic transformation of the signal and assuming a Gamma distribution. Section 3 outlines the proposed estimation method for the change point. The application of these techniques to real flight experimentation is detailed in Section 4, and Section 5 concludes the article, while discussing potential future research directions in this field.

II. GNSS-R Reflectivity Statistical Model

In a dual antenna configuration, a GNSS-R receiver utilizes a Right-Hand Circular Polarized (RHCP) antenna directed towards the zenith to receive direct signals from satellites, while a Left-Hand Circular Polarized (LHCP) antenna points towards the nadir for receiving reflected signals, as depicted in Fig. 1. In the GNSS-R radar observation system, reflectivity is determined by the ratio of the reflected signal intensity over the direct signal intensity. When dealing with a perfectly flat, dielectric surface, the reflected power is highly coherent as the GNSS signal reflects from the specular point, resulting in maximum reflected signal intensity.

Conversely, rough surfaces cause signals to scatter across a specific area before reaching the receiving antenna. An increase in surface roughness primarily results in a larger glistening zone, which divides the scattered power into two components: a specular coherent component and an incoherent component due to surface roughness. Within glistening zones, points with similar Doppler and range parameters to the specular point generate multiple reflections, introducing phase delays that must be considered in GNSS signal processing models.

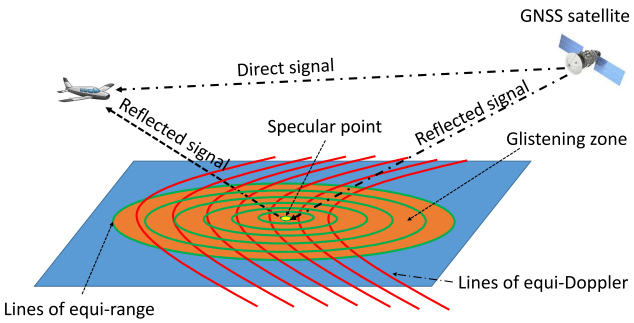

Fig. 1. GNSS-R radar observation system.

A. Direct and Reflected Signal Tracking

The study employs two tracking loops for satellite signals, using traditional Phase-Locked Loop (PLL) and Delay-Locked Loop (DLL) approaches for direct signal tracking and an extra Frequency-Locked Loop (FLL) for dynamic Doppler frequency changes. Two quadrature components are demodulated and correlated with local replicas to obtain two quadrature components of correlation, $I_d(0)$ and $Q_d(0)$ which are assumed to be random variables distributed according to Gaussian distributions:

$$I_d(0) \sim \mathcal{N}(a\cos(\phi_e), \sigma^2) \tag{1}$$

$$Q_d(0) \sim \mathcal{N}(a\sin(\phi_e), \sigma^2) \tag{2}$$

Using these two correlation components, we calculate the direct signal intensity as:

$$T_d = I_d^2(0) + Q_d^2(0) \tag{3}$$

The standard deviation, σ, of the Gaussian distribution is a function of the noise power in the direct signal. We can define the mean value of the direct signal intensity as:

$$\frac{T_d}{\sigma^2} \tag{4}$$

which follows a non-central chi-squared distribution of parameter a^2. Then we have:

$$E(T_d) = a^2 + 2\sigma^2 \tag{5}$$

In our implementation, we assume that the direct signal remains stationary for a significant duration, where we estimate its mean value.

The reflected signal tracking uses an assisted loop with pseudo-range and geometric model, considering Doppler frequency estimates from the direct signal [14]. It processes two quadrature components, where $I_r(0)$ and $Q_r(0)$ are assumed to follow a centered normal distribution with σ_r. We calculate the reflected signal intensity as:

$$T = I_r^2(0) + Q_r^2(0) \tag{6}$$

The mean value of the reflected signal intensity is $2\sigma_r^2$. In our implementation, we process the mean intensity of the received signal within a working window of size N.

$$T_r = \frac{1}{N}\sum_{i=1}^{N}\left(I_r^2(0) + Q_r^2(0)\right) \tag{7}$$

In this setup, increasing the size of the working window, N, boosts the Signal-to-Noise Ratio (SNR) of the intensity. For processing correlation components of the GPS L1 signal, $Tc = 1ms$ data, with N typically set to 20. As a result, the reflected signal intensity distribution follows a Gamma distribution:

$$T_r \sim \text{Gamma}\left(N, \frac{2\sigma_r^2}{N}\right) \tag{8}$$

where $2\sigma_r^2$ is the mean value of the intensity and $4\sigma_r^4/N$ represents its variance.

B. Reflectivity and Homomorphic Transformation of the GNSS-R Signal

In a GNSS-R radar system, the power of the reflected signal is a function of the power of the direct signal. To normalize the observation of the reflected signal, we use the expression of reflectivity, which is given by the following formula:

$$R = \frac{T_r}{E(T_d)} = \frac{\frac{1}{N}\sum_{i=1}^{N}\left(I_r^2(0) + Q_r^2(0)\right)}{a^2 + 2\sigma^2} \tag{9}$$

where $E(Td)$ represents the average intensity of the direct signal, assumed to remain constant throughout the duration of the experiment. In practice, the intensity of the direct signal changes slowly over time and its mean value can be easily estimated.

This paper suggests that the reflectivity R follows a Gamma distribution, based on the Goodman model [21], [22]. In this case, the noise affecting the observations is described as multiplicative speckle noise. Let:

$$R(N,\lambda) \sim Gamma\,(N, \lambda/N) \tag{10}$$

with:

$$E(R(N,\lambda)) = \lambda = \frac{2\sigma_r^2}{(a^2 + 2\sigma^2)} \tag{11}$$

The noise power in a multiplicative model is affected by the signal amplitude, which is transformed into additive noise using homomorphic log-operation, with constant power. The log-transform is defined by:

$$W(N,\lambda) = \log\left(R(N,\lambda)\right) \tag{12}$$

with:

$$W(N,\lambda) \sim Log - Gamma\,(N, \lambda/N) \tag{13}$$

We have the following expressions:

$$E(W(N,\lambda)) = \Psi(N) + \log(\lambda/N) \tag{14}$$

$$V(W(N,\lambda)) = \Psi^{(1)}(N) \tag{15}$$

where $V(W(N,\lambda))$, the variance of $W(N,\lambda)$, is constant, and $\Psi(\dots)$ and $\Psi^{(1)}(\dots)$ are respectively the digamma function and the trigamma function [23], [24].

III. Change Point Detection

In a radar application, we process a large amount of data sequentially as a chronological series. We consider this series to be in control when the statistical parameters of the process are stationary. In contrast, it is considered out of control in the non-stationary case when there is a change in the process. The hypothesis test for the change point detection is used to detect such changes in the process. It is defined as follows:

$$H_0 : R_t \sim \text{Log-Gamma}(N, \frac{\lambda_0}{N}) \quad \forall t \in \{1,\dots,n\} \tag{16}$$

$$H_\tau : R_t \sim \text{Log-Gamma}(N, \frac{\lambda_0}{N}) \quad \forall t \in \{1,\dots,\tau\} \tag{17}$$

$$R_t \sim \text{Log-Gamma}(N, \frac{\lambda_1}{N}) \quad \forall t \in \{\tau+1,\dots,n\} \tag{18}$$

with $\lambda_0 \neq \lambda_1$ and $\tau \in \{1,\dots,n-1\}$, the instant of the change. Fig. 2 provides an overview of the signal model within the working window N under H_τ. It illustrates the transition between mean values λ_0 and λ_1 between different segments associated to different areas of reflection.

A. Change Point Detection Approach

The proposed change point detector aims to identify changes in the observed process. Fig. 3 depicts the flowchart of the on-line/off-line change point detector.

The proposed filter involves a recursive mean estimate derived from the log-transformation of the reflectivity observations; this estimate can be expressed as a function of the innovation i_t as:

$$\bar{w}_t = \bar{w}_{t-1} + \alpha_{2,t}\; i_t \tag{19}$$

$$i_t = \log(r_t) - \bar{w}_{t-1} \tag{20}$$

The optimal expression of $\alpha_{2,t}$ is given in a recursive form, evolving toward a constant value, and the smoothing of the mean estimate, $\bar{w}_t$, increases until a constant smoothing level. The CUSUM detector, in its simple form, is expressed as:

$$P_t = \frac{(P_{t-1} + Q)\,\Psi^{(1)}(N)}{P_{t-1} + Q + \Psi^{(1)}(N)} \tag{21}$$

$$\alpha_{2,t} = \frac{P_t}{\Psi^{(1)}(N)} \tag{22}$$

where Q is a parameter defined by the user, and P_t the variance of the estimate $\bar{w}_t$. The normalized innovation is defined as:

$$\tilde{i}_t = \frac{i_t}{P_{t-1} + \Psi^{(1)}(N)}. \tag{23}$$

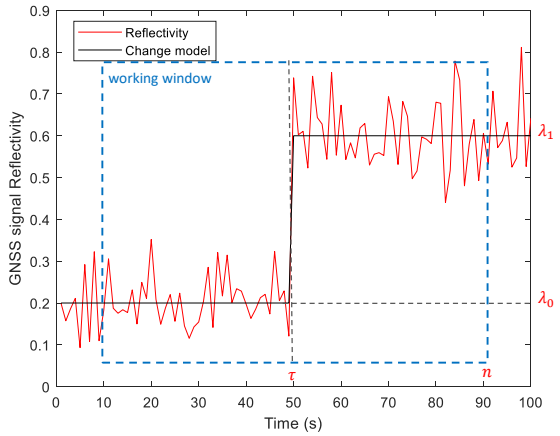

Fig. 2. Transition model in a working window.

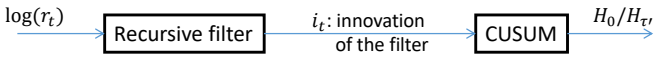

Fig. 3. Change point detection system.

The localization of the change is then processed within a working window centered on τ', the detected instant of change. We have:

$$g_t^+ = \left(g_{t-}^+ + \tilde{i}_t\right)^+ \tag{24}$$

$$g_t^- = \left(g_{t-}^- - \tilde{i}_t\right)^+ \tag{25}$$

$$\tau' = \min\left\{k : (g_t^+ \geq C_s) U (g_t^- \geq C_s)\right\} \tag{26}$$

Before the change, the integration of the innovation process behaves as a random walk, denoted by g_k^+ and g_k^-. After the change occurs at time $\tau + t$, both g_k^+ and g_k^- transition into monotonic increasing functions. C_s is the user-defined threshold, determining the probability of false alarm under H_0. The proposed change point estimate corrects the delay between the change instant and the alarm instant under H_τ.

B. Change Point Estimation Approach

The observations of reflectivity, denoted as r_t, are transformed into samples $w_t = \log(r_t)$. These samples follow a Log-Gamma distribution, expressed by:

$$f(W_t; N, \lambda/N) = \frac{(e^{W_t})^N e^{-\frac{N e^{W_t}}{\lambda}}}{\left(\frac{\lambda}{N}\right)^N \Gamma(N)} \tag{27}$$

Consider a set of n i.i.d. samples $W_{1:n} = (W_1, \ldots, W_n)$ distributed according to the Log-Gamma$(N, \lambda/N)$ distribution, defining the working window depicted in Fig. 2. The associated log-likelihood function, denoted as $l(W_{1:n}; N, \lambda/N)$, is given by:

$$l(W_{1:n}; N, \lambda/N) = N \sum_{i=1}^{n} W_i - \frac{N}{\lambda} \sum_{i=1}^{n} e^{W_i} - nN \log\left(\frac{\lambda}{N}\right) - n \log(\Gamma(N)) \tag{28}$$

The estimate of λ, denoted as $\hat{\lambda}$, is determined by:

$$\hat{\lambda} = N e^{(\overline{W} - \Psi(N))} \tag{29}$$

where:

$$\overline{W} = \frac{1}{n} \sum_{i=1}^{n} W_i \tag{30}$$

Define the generalized log-likelihood function as $l(W_{1:n}; N, \hat{\lambda}/N)$. The change point localization, denoted as $\hat{\tau}$, is estimated by maximizing the sum of log-likelihood:

$$\hat{\tau} = \underset{0<\tau<n}{\arg\max} \Big[l(W_{1:\tau}; N, \hat{\lambda}_0/N) + l(W_{\tau+1:n}; N, \hat{\lambda}_1/N) \Big]$$

where $\hat{\lambda}_0$ and $\hat{\lambda}_1$ are estimates based on the samples $W_{1:\tau}$ and $W_{\tau+1:n}$, respectively.

C. Parameter definitions

To ensure the reproducibility of the signals segmentation, the parameters of both the change point detector and change point estimate must be independent of the parameters and of the direct signal intensity (a and σ) and the reflected signal intensity (σ_r).

For the change point detector, we suggest fixing the threshold C_s as a function of the probability of false alarm rate. In change point detection, the false alarm rate is characterized by the ARL under H_0, denoted as ARL(0). ARL(0) is the expected number of observations between false alarms in a sequence of observations that represents noise without a change point. The value of ARL(0) is determined by simulation with a noise power $\sqrt{\Psi^{(1)}(N)}$ under H_0. The noise power defined by N is independent of the direct and reflected signal intensity.

The accuracy of the change point estimate relies only on the precision of estimating $\overline{W}$. This precision is determined by the noise power $\sqrt{\Psi^{(1)}(N)}$ and remains independent of the direct and reflected signal intensity.

IV. Experimentation: Application to Airborne GNSS-R data

A. Flight Information

Airborne GNSS-R data was recorded during a flight experimentation on October 19, 2020 in the Northern Region of France, starting at 14:45 Coordinated Universal Time (UTC). The experimental setup employed a gyrocopter equipped with RHCP antenna for direct signal reception and LHCP antenna for receiving reflected signals. The gyrocopter took off from Calais–Dunkerque Airport with a variety of embedded sensors, including a drone board sensor for recording essential parameters.

The flight covered a wide region of around 230 km^2 in about 45 minutes. With an average speed of 95 km/h and a cruise height of 315 m, the gyrocopter flew over 50 various inland water body surfaces as well as sandy beach and the sea. The research focused on reflections from satellites with high elevation angles; the satellite footprints during this flight are shown in Fig. 4.

B. Analyzing the Log Transform Noise Model

One of the main contributions of this article is the derivation of a detection threshold that can be applied to different datasets. Our approach relies on the assumption that the log-transform of reflectivity follows a Log-Gamma distribution, enabling the definition of a detection threshold independent of the SNR. To validate this assumption, we estimate the noise power using real airborne GNSS-R reflectivity data, as illustrated in Fig. 5.

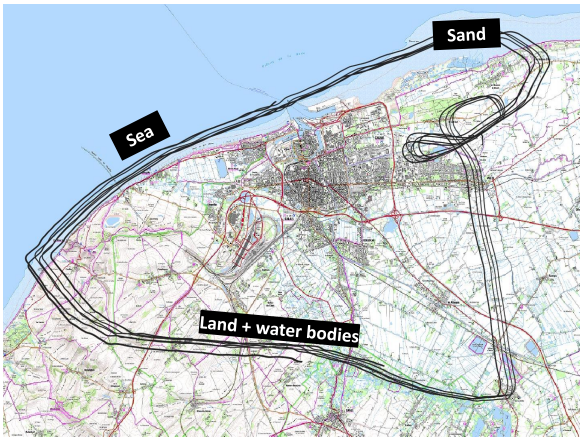

Fig. 4. The traces of the satellites with high elevation angles along the trajectory.

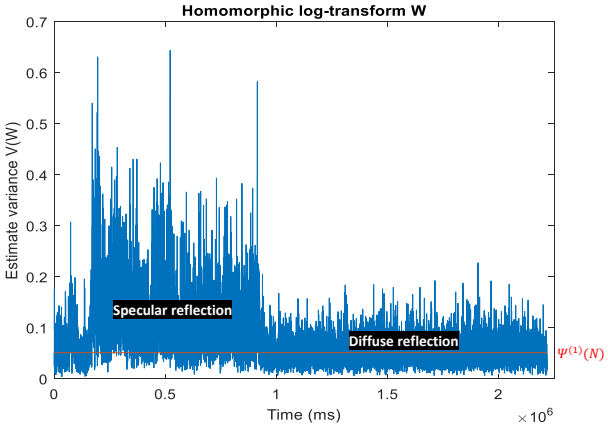

Fig. 5. Estimation of the Homomorphic log-transform variance.

This figure shows the variance of reflectivity log-transform estimates from 10 samples processed for the satellite PRN 5 trace. There are two distinct reflecting areas: one with specular reflections related to sand and sea, and another with diffuse reflections associated with plain land. The red line corresponds to the theoretical variance of the log-transform and closely matches the average variance in the second region. However, it's essential to note that in real-world scenarios, the distribution of specular reflections may not follow a specific theoretical model due to the complex and changing environmental conditions.

The threshold is fixed for the diffuse reflections area, i.e. land region. However, the probability of false alarm detection may increase in areas characterized by coherent reflections from water surfaces, due to the increase in the standard deviation of that particular area.

C. Change Point Estimation

In Fig. 6, we display reflectivity measurements from airborne GNSS signals during the flight over three water bodies.

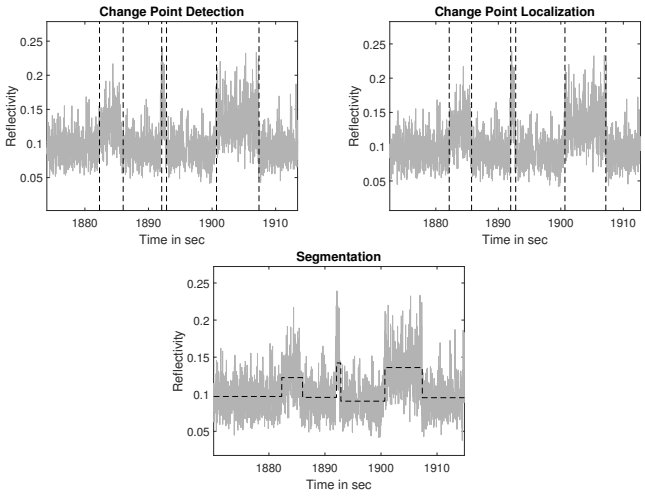

Fig. 6. Change point process: Detection, Localization and Segmentation.

The variations in GNSS signal reflectivity are processed using change detection algorithms. The CUSUM algorithm is initially employed to detect reflectivity changes, with parameters set to ARL(0) = 3000 for N=20 and smoothing parameter $Q = 0.001$. Changes with dynamic values below 0.01 are filtered out to reduce false alarms in specular reflection areas. After CUSUM detection, our proposed Log-Gamma Maximum Likelihood (LGML) localization is applied to precisely locate these changes. Finally, the signal is segmented into sections, each corresponding to changes in mean reflectivity levels based on localized change points as shown in Fig. 6.

D. Segmentation

We apply our radar signal segmentation technique for detecting in-land water bodies, as depicted in Fig. 7, representing the radar signal segmentation for airborne GNSS measurements along the trajectory of the flight. The Google Earth image illustrate satellite footprints, color-coded with yellow denoting land and blue indicating water bodies based on mean reflectivity measurements. These colors are associated with different mean reflectivity values. The GNSS reflectivity measurements for three satellites (PRN 5, 7, and 30), each characterized by a different elevation angle, are analyzed.

Surface reflectivity shows a direct correlation with water content in land, with reflectivity increasing when signals are reflected from water bodies. Additionally, the noise variance increases with the mean reflectivity. The radar technique detects in-land water bodies of various sizes and shapes under different environments, showcasing its capability to differentiate surfaces.

E. K-Means Automatic Classification

We apply K-means clustering technique, an unsupervised machine learning method, to classify reflectivity signal segments based on their statistical properties, the mean

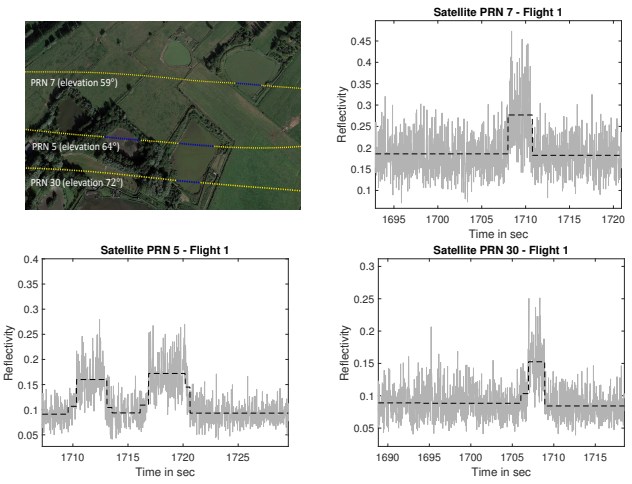

Fig. 7. Segmentation of the GNSS measurements

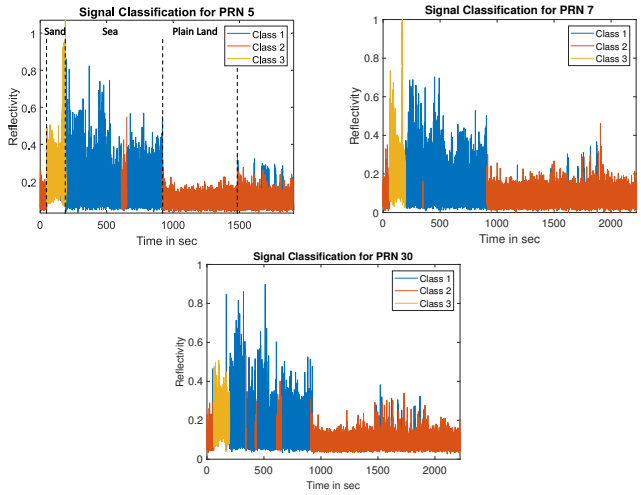

Fig. 8. Reflectivity Classification for the different satellites.

and standard deviation. Each segment represents a distinct portion of the GNSS reflectivity signal. The K-means method initializes cluster centers randomly, assigns segments to the nearest cluster based on feature similarity, and updates cluster centers by calculating mean values. The iterative process continues until convergence.

Fig. 8 illustrates the classification results for our flight, where the reflectivity signal is categorized into three main classes in coherence with the locations of the sandy beach, sea and land of Figure 4. These areas were determined using ground truth observations, Google Earth imagery, and accurate IGN (Institut Geographique National) maps. The results of the three reflectivity signals are in alignment highlighting the consistency of the automatic classification technique.

F. Percentage of Overlapping of GNSS-R Reflectivity Signals

The overlapping percentage is defined as a quantitative measure used to evaluate the consistency of the GNSS-R classification methodology across the different studied satellite signals. It is computed as the percentage of samples, for a given PRN, that result in the same classification as those of the reference signal of PRN 5. This percentage is computed, for each class, in the sections defined in the signal classification for PRN 5 in Fig. 8.

TABLE I
PERCENTAGE OF OVERLAPS OF GNSS-R REFLECTIVITY SIGNALS

		Land	Sea	Sand
FLIGHT 1	PRN 5	100	100	100
	PRN 7	99.67	99.82	98.49
	PRN 30	99.67	97.26	94.75

Based on the results shown in the table, it is clear that during Flight 1, all three satellites show significant overlap percentages for both land and sea classes. The values range from 97.26% to 99.67%. The high percentages suggest a strong agreement between the reflectivity signals acquired from these satellites with respect to the reference signal, PRN 5, for land and sea surfaces. However, there is a slight decrease in the overlap percentages observed in the sand class, specifically for PRN 30, where the percentage decreases to 94.75%. It is important to note that the traces followed by the three satellites are not the same, and thus the reflectivity measurements vary depending on the reflecting surface characteristics and the detection length by the satellites. The differences in azimuth angles can also contribute to this difference.

V. CONCLUSION

This paper presents algorithms designed to detect and accurately localize change points in GNSS-R reflectivity data. These algorithms are specifically developed for dealing with the challenges associated with multiplicative speckle noise following the Gamma model distribution. Our approach demonstrates strong segmentation capabilities while combining a CUSUM change point detector with a Maximum Likelihood localization algorithm that relies on log-transformed reflectivity data. Our algorithms successfully identify different land features through real flight experiment conducted in the Northern Region of France. Applying K-means clustering for classification, we accurately differentiate between sand, water bodies, and plain land. Our study contributes to the development of GNSS-R technology and opens a path for future research in enhancing surface classification methods for wider remote sensing applications.

ACKNOWLEDGMENT

The authors would like to thank the CPER IDEAL program (approche Intégrée des Défis maritimes et Littoraux) for their financial support.

REFERENCES

[1] Kegen Yu, Chris Rizos, Derek Burrage, Andrew G Dempster, Kefei Zhang, and Markus Markgraf, "An Overview of GNSS Remote Sensing," *EURASIP Journal on Advances in Signal Processing*, vol. 2014, pp. 1–14, 2014.

[2] Kegen Yu, Shuai Han, Jinwei Bu, Yuhang An, Zhewen Zhou, Changyang Wang, Sajad Tabibi, and Joon Wayn Cheong, "Spaceborne GNSS Reflectometry," *Remote Sensing*, vol. 14, no. 7, pp. 1605, 2022.

[3] Zheng Li, Fei Guo, Fade Chen, Zhiyu Zhang, and Xiaohong Zhang, "Wind Speed Retrieval using GNSS-R Technique with Geographic Partitioning," *Satellite Navigation*, vol. 4, no. 1, pp. 4, 2023.

[4] James L Garrison and Stephen J Katzberg, "The Application of Reflected GPS Signals to Ocean Remote Sensing," *Remote Sensing of Environment*, vol. 73, no. 2, pp. 175–187, 2000.

[5] James L Garrison, Attila Komjathy, Valery U Zavorotny, and Stephen J Katzberg, "Wind Speed Measurement using Forward Scattered GPS Signals," *IEEE Transactions on Geoscience and Remote Sensing*, vol. 40, no. 1, pp. 50–65, 2002.

[6] Estel Cardellach and Antonio Rius, "A New Technique to Sense Non-Gaussian Features of the Sea Surface from L-Band Bi-static GNSS Reflections," *Remote Sensing of Environment*, vol. 112, no. 6, pp. 2927–2937, 2008.

[7] Roberto Sabia, Marco Caparrini, Adriano Camps, and Giulio Ruffini, "Potential Synergetic Use of GNSS-R Signals to Improve the Sea-state Correction in the Sea Surface Salinity Estimation: Application to the SMOS mission," *IEEE Transactions on Geoscience and Remote Sensing*, vol. 45, no. 7, pp. 2088–2097, 2007.

[8] Manuel Martin-Neira, "A Passive Reflectometry and Interferometry System (PARIS): Application to Ocean Altimetry," *ESA journal*, vol. 17, no. 4, pp. 331–355, 1993.

[9] Shuanggen Jin, Xiaodong Qian, and Xuerui Wu, "Sea Level Change from BeiDou Navigation Satellite System-Reflectometry (BDS-R): First Results and Evaluation," *Global and Planetary Change*, vol. 149, pp. 20–25, 2017.

[10] Maria Belmonte Rivas, James A Maslanik, and Penina Axelrad, "Bistatic Scattering of GPS Signals off Arctic Sea Ice," *IEEE Transactions on Geoscience and Remote Sensing*, vol. 48, no. 3, pp. 1548–1553, 2009.

[11] Joakim Strandberg, Thomas Hobiger, and Rüdiger Haas, "Coastal Sea Ice Detection using Ground-Based GNSS-R," *IEEE geoscience and remote sensing letters*, vol. 14, no. 9, pp. 1552–1556, 2017.

[12] Estel Cardellach, Fran Fabra, Antonio Rius, Simone Pettinato, and Salvatore D'Addio, "Characterization of Dry-Snow Sub-structure using GNSS Reflected Signals," *Remote Sensing of Environment*, vol. 124, pp. 122–134, 2012.

[13] Nereida Rodriguez-Alvarez, Albert Aguasca, Enric Valencia, Xavier Bosch-Lluis, Isaac Ramos-Pérez, Hyuk Park, Adriano Camps, and Merce Vall-Llossera, "Snow Monitoring using GNSS-R Techniques," in *2011 IEEE International Geoscience and Remote Sensing Symposium*. IEEE, 2011, pp. 4375–4378.

[14] Hamza Issa, Georges Stienne, Serge Reboul, Mohamad Raad, and Ghaleb Faour, "Airborne GNSS Reflectometry for Water Body Detection," *Remote Sensing*, vol. 14, no. 1, pp. 163, 2021.

[15] Frédéric Frappart, Pierre Zeiger, Julie Betbeder, Valéry Gond, Régis Bellot, Nicolas Baghdadi, Fabien Blarel, José Darrozes, Luc Bourrel, and Frédérique Seyler, "Automatic Detection of Inland Water Bodies along Altimetry Tracks for Estimating Surface Water Storage Variations in the Congo Basin," *Remote Sensing*, vol. 13, no. 19, pp. 3804, 2021.

[16] Mehrez Zribi, Dominique Guyon, Erwan Motte, Sylvia Dayau, Jean-Pierre Wigneron, Nicolas Baghdadi, and Nazzareno Pierdicca, "Performance of GNSS-R GLORI Data for Biomass Estimation over the Landes forest," *International Journal of Applied Earth Observation and Geoinformation*, vol. 74, pp. 150–158, 02 2019.

[17] Stephen J Katzberg, Omar Torres, Michael S Grant, and Dallas Masters, "Utilizing Calibrated GPS Reflected Signals to Estimate Soil Reflectivity and Dielectric Constant: Results from SMEX02," *Remote sensing of environment*, vol. 100, no. 1, pp. 17–28, 2006.

[18] Brian W Barrett, Edward Dwyer, and Pádraig Whelan, "Soil moisture retrieval from active spaceborne microwave observations: An evaluation of current techniques," *Remote Sensing*, vol. 1, no. 3, pp. 210–242, 2009.

[19] Rayan Imam, Marco Pini, Gianluca Marucco, Fabrizio Dominici, and Fabio Dovis, "UAV-based GNSS-R for Water Detection as a Support to Flood Monitoring Operations: A Feasibility Study," *Applied Sciences*, vol. 10, no. 1, pp. 210, 2019.

[20] Alfredo Favenza, Rayan Imam, Fabio Dovis, and Marco Pini, "Detecting Water using UAV-based GNSS-Reflectometry Data and Artificial Intelligence," in *2019 IEEE International Workshop on Metrology for Agriculture and Forestry (MetroAgriFor)*. IEEE, 2019, pp. 7–12.

[21] Joseph W Goodman, "Statistical Properties of Laser Speckle Patterns," in *Laser speckle and related phenomena*, pp. 9–75. Springer, 1975.

[22] Chris Oliver and Shaun Quegan, *Understanding Synthetic Aperture Radar Images*, SciTech Publishing, 2004.

[23] Leigh J. Halliwell, "The Log-Gamma Distribution and Non-Normal Error by," 2018.

[24] Ross L Prentice, "A Log Gamma Model and Its Maximum Likelihood Estimation," *Biometrika*, vol. 61, no. 3, pp. 539–544, 1974.